

See discussions, stats, and author profiles for this publication at: <https://www.researchgate.net/publication/221816400>

# Interfacial Properties and Iron Binding to Bacterial Proteins That Promote the Growth of Magnetite Nanocrystals: X-ray Reflectivity and Surface Spectroscopy Studies

ARTICLE *in* LANGMUIR · MARCH 2012

Impact Factor: 4.46 · DOI: 10.1021/la205074n · Source: PubMed

---

CITATIONS

18

---

READS

15

7 AUTHORS, INCLUDING:



Pierre Palo

Iowa State University

13 PUBLICATIONS 308 CITATIONS

SEE PROFILE



Surya K Mallapragada

Iowa State University

171 PUBLICATIONS 3,012 CITATIONS

SEE PROFILE



Marit Nilsen-Hamilton

Iowa State University

120 PUBLICATIONS 2,892 CITATIONS

SEE PROFILE



David Vaknin

Iowa State University

248 PUBLICATIONS 5,925 CITATIONS

SEE PROFILE

# Interfacial Properties and Iron Binding to Bacterial Proteins That Promote the Growth of Magnetite Nanocrystals: X-ray Reflectivity and Surface Spectroscopy Studies

Wenjie Wang,<sup>†</sup> Wei Bu,<sup>†</sup> Lijun Wang,<sup>‡</sup> Pierre E. Palo,<sup>‡</sup> Surya Mallapragada,<sup>§</sup> Marit Nilsen-Hamilton,<sup>‡</sup> and David Vaknin<sup>\*,†</sup>

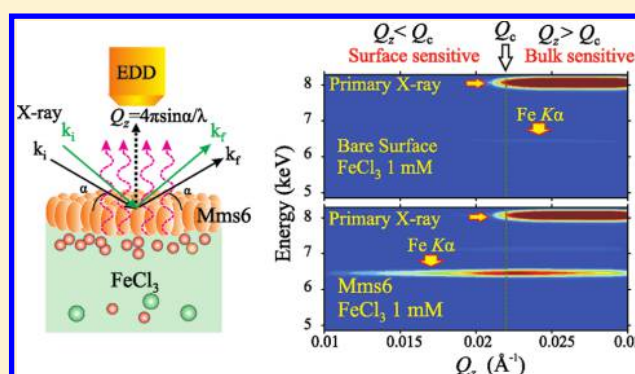
<sup>†</sup>Ames Laboratory, and Department of Physics and Astronomy, Iowa State University, Ames, Iowa 50011, United States

<sup>‡</sup>Ames Laboratory, and Department of Biochemistry, Biophysics and Molecular Biology, Iowa State University, Ames, Iowa 50011, United States

<sup>§</sup>Ames Laboratory, and Department of Chemical and Biological Engineering, Iowa State University, Ames, Iowa 50011, United States

## Supporting Information

**ABSTRACT:** Surface sensitive X-ray scattering and spectroscopic studies have been conducted to determine structural properties of Mms6, the protein in *Magnetospirillum magneticum* AMB-1 that is implicated as promoter of magnetite nanocrystals growth. Surface pressure versus molecular area isotherms indicate Mms6 forms stable monolayers at the aqueous/vapor interface that are strongly affected by ionic conditions of the subphase. Analysis of X-ray reflectivity from the monolayers shows that the protein conformation at the interface depends on surface pressure and on the presence of ions in the solutions, in particular of iron ions and its complexes. X-ray fluorescence at grazing angles of incidence from the same monolayers allows quantitative determination of surface bound ions to the protein showing that ferric iron binds to Mms6 at higher densities compared to other ions such as Fe<sup>2+</sup> or La<sup>3+</sup> under similar buffer conditions.



## INTRODUCTION

Iron oxide compounds have been widely used throughout human history as pigments, catalysts, electronic recording devices, and numerous other applications.<sup>1</sup> Nanoparticles of magnetic iron oxides such as magnetite Fe<sub>3</sub>O<sub>4</sub> and maghemite γ-Fe<sub>2</sub>O<sub>3</sub> have gained interest recently due to their potential applications in medicine and biology in general.<sup>2</sup> One route to control nanocrystal growth of magnetite and similar compounds is to mimic in the laboratory the biomineralization processes used by magnetotactic bacteria, for example *Magnetospirillum magneticum* AMB-1. This bacterium uses an array of magnetosomes, encapsulated magnetite nanocrystals, to navigate through aquatic oxygen gradients.<sup>1</sup> To date, many aspects of in vivo biomineralization mechanisms of magnetite nanocrystal formation in the bacterial magnetosomes including iron transport, catalytic reduction of Fe(III) to Fe(II), and control of particle size and shape, still remain highly debated and no universal models have been reached.<sup>3</sup> Nevertheless, Mms6, a relatively small polypeptide consisting of only 59 amino acids, appears to play a role in regulating and controlling magnetite particle growth in vivo. Mms6 is tightly bound to the surfaces of cuboidal magnetite particles that are isolated from *Magnetospirillum magneticum* AMB-1.<sup>4–7</sup> Chemical synthesis of magnetite particles by coprecipitation of Fe(III) and Fe(II) shows that the presence of Mms6 proteins mediates the formation of

cuboidal magnetite particles of narrow size distribution (range 20–30 nm),<sup>6</sup> which opens a new door to synthetic methodologies of preparing nanoparticles of specific type, shape, and morphology. Mms6 has a number of carboxyl and hydroxyl groups side chains, both of which are capable of binding iron and other metal ions. Indeed, the carboxyl- and hydroxyl-rich regions have been considered as the active iron binding sites where growth of magnetite is presumably initiated.<sup>4</sup> Accumulating 2D and 3D iron nanoparticles assemblies to ideal 2D templates of carboxyl or hydroxyl groups has been investigated by employing Langmuir monolayers consisting of densely packed amphiphilic molecules such as arachidic acid (AA), each with a carboxyl headgroup oriented toward the aqueous media and a hydrocarbon tail away from the aqueous media. A single- or multilayer of iron (hydr)oxides can grow contiguously to the monolayer when the conditions of the aqueous media, such as pH, iron constituents, and buffering materials are regulated.<sup>8–10</sup> Of particular interest is a study at ambient conditions that demonstrates that magnetite can grow under AA monolayer on a FeCl<sub>2</sub> subphase at a nearly neutral pH (~6.6), when purged with oxygen as oxidants for Fe<sup>2+</sup>.<sup>8</sup> Similar studies

Received: December 22, 2011

Revised: February 3, 2012

Published: February 8, 2012



reflectivity can also be calculated by using a recursive dynamical method<sup>26</sup> as we do in this study. The symbols  $Q_z$  and  $\alpha_i$  are used interchangeably in this paper. The interpretation of reflectivity data is based on the effective-density model,<sup>27</sup> which has been successfully used to study iron nanoparticles and proteins adsorption at the air/water interface.<sup>12,28,29</sup> The ED profile  $\rho(z)$  constructed using the effective-density model is sliced into a histogram of  $M$  thin slabs of constant thickness. The reflectivity is then calculated by the Parratt formalism with  $M \sim 100$  and a uniform slab thickness  $\sim 1$  Å (more details can be found in Supporting Information).<sup>30</sup>

The amount and volume fraction of absorbed proteins at the air–water interface can be estimated based on ED profiles, assuming the adsorbed layer(s) is a mixture of the protein and subphase solution.<sup>23,29,31,32</sup> The volume fraction profile of adsorbed Mms6,  $\Phi_{\text{Mms6}}(z)$ , can be directly related to  $\rho(z)$  as follows<sup>29</sup>

$$\Phi_{\text{Mms6}}(z) = \frac{\rho(z) - \rho_{\text{ref}}(z)}{\rho_{\text{protein}} - \rho_{\text{ref}}(z)} \quad (2)$$

where  $\rho_{\text{ref}}(z)$  is the ED profile obtained by replacing the adsorbed proteins with the subphase solution. The ED of the dehydrated proteins,  $\rho_{\text{protein}}$  is estimated to be  $0.455 \pm 0.013 \text{ e/Å}^3$  for Mms6 based on average density of proteins ( $\sim 1.40 \pm 0.04 \text{ g/cm}^3$ , MW  $\sim 10 \text{ kDa}$ ).<sup>33</sup> The mass of adsorbed proteins per surface area,  $\Gamma_s$ , can be derived from obtained volume fraction profile  $\Phi_{\text{Mms6}}(z)$ .<sup>29</sup>

X-ray fluorescence (XF) from the films as a function of the X-ray incident-angle  $\alpha_i$  (or corresponding  $Q_z$ ), using a Vortex energy dispersive detector (EDD), is used to determine quantitatively the density of specific ions that accumulate at the interface.<sup>34</sup> The pencil-like detector for collecting fluorescence is pointed directly at the surface separated by a Kapton window in an aluminum well protruding into the Langmuir trough container (about 2 cm away from the liquid surface). An illustration of the fluorescence setup is depicted in part c of Figure 1. The fluorescence from pure water serves as background and is subtracted from all data to remove electronic noise, stray signals and escape peak (due to the  $K_\alpha$  excitation of Si: the main component of the detector). The fluorescence from the subphase of known ionic concentration is used to normalize the detected intensity to the number of emitting ions. One of the advantages of X-ray near total external reflection fluorescence technique is its high surface sensitivity. This can be explained and illustrated by examining the X-ray Fresnel reflectivity,  $R_F$ , from a sharp, flat air/water interface, as shown in Figure 2.

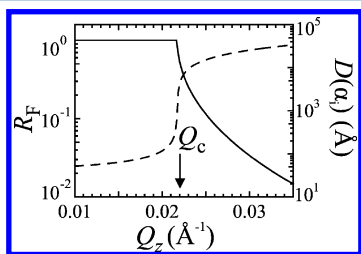


**Figure 2.** Fresnel reflectivity  $R_F$  (solid line) and X-ray penetration depth  $D(\alpha_i)$  (dashed line) for a flat, sharp surface of pure water as a function of  $Q_z$  calculated for X-ray energy  $E = 8 \text{ keV}$ . When  $Q_z$  is below  $Q_c$ , the reflectivity is unity.

Below the critical angle  $\alpha_c$  (corresponding to  $Q_z = Q_c$ ) for total external reflection, the reflectivity is unity and the X-ray penetration depth normal to the surface,  $D(\alpha_i)$ , is no more than  $\sim 100$  Å at 80% of critical angle  $\alpha_c$ . Above the critical angle, the X-ray penetrates into the bulk, and is attenuated by absorption and scattering processes. Another advantage of the X-ray fluorescence technique is its element specificity. When an X-ray wave travels through the surface and into the solution, each excited element in its path gives out characteristic emission lines that can be identified among the various elements in solutions (for instance, in our case, Fe, La, Cl, and K).

To quantify the amount of a specific element at the surface and its spatial distribution, the intensity of the characteristic emission lines

of the element is integrated at each  $Q_z$ . For iron, at each  $Q_z$ , the fluorescence intensity is integrated over 6.1–6.7 keV range, denoted as  $I_F$ , to contain exclusively Fe  $K_\alpha$  ( $\sim 6.4 \text{ keV}$ ) emission line. The fluorescence intensity  $I_F$  as a function of  $\alpha_i$  (and corresponding  $Q_z$ ) can be expressed as follows:<sup>35,36</sup>

$$\begin{aligned} I_F(\alpha_i) &= C f_{\text{geom}}(\alpha_i) \int_0^\infty n_{\text{ion}}(z) |E(z)|^2 dz \\ &= C f_{\text{geom}}(\alpha_i) |t(\alpha_i)|^2 \int_0^\infty \{ [n_{\text{ion}}(z) - n_b] + n_b \} \\ &\quad \times \exp[-|z|/D(\alpha_i)] dz \\ &= \underbrace{C f_{\text{geom}}(\alpha_i) |t(\alpha_i)|^2 \int_0^\infty n_s(z) \exp[-|z|/D(\alpha_i)] dz}_{I_s(\alpha_i) - \text{surface}} \\ &\quad + \underbrace{C f_{\text{geom}}(\alpha_i) |t(\alpha_i)|^2 D(\alpha_i) n_b}_{I_b(\alpha_i) - \text{bulk}} \end{aligned} \quad (3)$$

where  $C$  is a scale factor,  $f_{\text{geom}}$  is a geometrical correction factor,  $n_{\text{ion}}(z)$  is the number distribution of ions (in unit of  $\text{Å}^{-3}$ ) across the interface ( $z$ -axis normal to the surface with origin at air/monolayer interface and increasing into the bulk).  $n_s(z)$  is the distribution of surface excess ions (decaying to zero away from the surface), and  $n_b$  is the bulk ionic concentration.  $E(z)$  is the electric field at depth  $z$ .  $t(\alpha_i)$  and  $D(\alpha_i)$  are electric field amplitude transmission coefficient at an air/water interface<sup>27,37</sup> and X-ray penetration depth normal to the surface,<sup>38</sup> respectively. For a bare surface solution, the fluorescence intensity, denoted as  $I_b$ , has a contribution only from the bulk, and this expression is employed to model the fluorescence intensity from the  $\text{FeCl}_3$  solution of bare surface. In the presence of a soft film on the aqueous surface, the increase in measured  $I_F$  with respect to  $I_b$ , denoted by  $I_s$  ( $I_s \equiv I_F - I_b$ ), is attributed to the surface bound ions. The surface density of bound iron in terms of number of iron atoms per  $\text{Å}^2$ ,  $n_{\text{Fe}} = \int n_s(z) dz$ , can be obtained directly by using the fluorescence signals data for  $\alpha_i > \alpha_c$  as follows

$$n_{\text{Fe}} = \frac{I_s(\alpha_i)}{I_b(\alpha_i)} D(\alpha_i) n_b \quad (4)$$

This formula is applied at each  $\alpha_i$  ( $> \alpha_c$ ) to obtain values of  $n_{\text{Fe}}$  independently and then averaged for all  $\alpha_i$ 's, as has been done elsewhere.<sup>39</sup>

X-ray absorption near edge structure spectroscopy (XANES) measures the energy dependence of absorption coefficient  $\mu(E)$  for a specific element near its main absorption edge. It can be obtained in the fluorescence geometry to probe the electronic-configuration, oxidation state (i.e., valence), and coordination chemistry of ion at the surface and in the bulk at  $Q_z = 0.018 \text{ Å}^{-1}$  and  $Q_z = 0.05 \text{ Å}^{-1}$ , respectively. As the intensity of Fe  $K_\alpha$  fluorescence line is proportional to  $\mu(E)$  for Fe, the XANES measurements are conducted by using the same instrumental setup as fluorescence measurements and by tuning the X-ray energy between 7.1 and 7.15 keV at constant  $Q_z$ . The XANES signal is constructed by integrating over the Fe  $K_\alpha$  emission line as a function of X-ray energy  $E$ . The XANES spectra are characterized by three major features, namely pre-edge, main absorption crest and spectral shape above the absorption edge. In this study, the energy shift of the main absorption edge is used to distinguish the oxidation states of iron in the bulk and at the surface.

The curve-fitting of the X-ray reflectivity and fluorescence data represented by symbols (circles, squares, etc.) and associated error bars due to counting statistics, is based on parametrized models and carried out through nonlinear least-squares method. The  $\chi^2$  is defined as the sum square of difference between model-dependent calculation and experimental data weighted by the uncertainty. The refinement of parameters is carried out through minimization of  $\chi^2$  to its minimum value  $\chi^2_{\text{min}}$ .



## RESULTS AND DISCUSSION

**Surface Pressure vs Area:  $\Pi$ –A Isotherms.** Figure 3 shows compression isotherms of surface pressure ( $\Pi$ ) versus

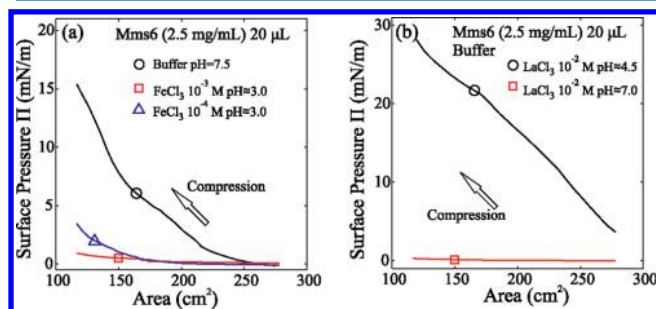


**Figure 3.** Compression isotherms of surface pressure  $\Pi$  vs surface area available to 20  $\mu$ L Mms6 proteins (2.5 mg/mL) spread on (a) the pure buffer solution, 1 mM and 0.1 mM buffered  $\text{FeCl}_3$  solutions at various pH as indicated; (b) 10 mM buffered  $\text{LaCl}_3$  solutions at various pH as indicated.

surface area ( $A$ ) for Mms6 on buffer and  $\text{FeCl}_3$  (part a of Figure 3) and  $\text{LaCl}_3$  (part b of Figure 3) at various concentrations and pH values, obtained after depositing 20  $\mu$ L of 2.5 g/L Mms6. We find that the isotherms are highly reproducible when the same amount of same concentration is spread on the surface. However, isotherms depend on the amount of Mms6 that is spread, which is indicative of micelle formation above a critical protein concentration. Assuming all the spread proteins remain on the surface, the nominal surface excess of Mms6 is estimated as  $\Gamma_s = 5 \times 10^{-4}$  mg/cm<sup>2</sup> (for 50  $\mu$ g spread over  $\sim 100$  cm<sup>2</sup> of surface area). On the basis of the change in the slope of the  $\Pi$ – $\Gamma_s$  isotherms into a plateau region observed by increasing the amount of Mms6 spread at the interface, we estimate a nominal saturation surface excess  $\Gamma_s^{\text{max}} = (30 \pm 5) \times 10^{-4}$  mg/cm<sup>2</sup> from which we estimate the critical micelle concentration (CMC) is at approximately  $1.5 \times 10^{-7}$  M (at pH = 7.5). The more realistic  $\Gamma_s$  can be estimated from  $R/R_F$  as discussed in the X-ray Reflectivity section. Figure 3 also shows that the isotherms depend on the presence of ions in the solution. For the same amount of Mms6 spread over the aqueous surface of  $\text{FeCl}_3$  solutions, the surface pressure at the lowest surface area is much lower than that for Mms6 on the buffer solution alone. Part a of Figure 3 also shows that, the higher the subphase iron concentration, the smaller the surface pressure increases upon film compression. This is a strong indication of iron interacting with the protein

presumably causing more compact folding of the protein upon iron binding. For comparison, the isotherms of  $\text{LaCl}_3$  buffer solutions show a similar trend, the surface pressure remains negligibly low for 10 mM  $\text{La}^{3+}$  at pH  $\sim 7.0$  when X-ray measurement shows that significant binding of  $\text{La}^{3+}$  occurs. We attribute these trends to the properties of carboxyl groups ( $\text{pK}_a$  5.3) as well as to different ionic behaviors as a function of pH.<sup>9,10</sup>

**X-ray Reflectivity.** Two XR measurements were conducted separately when Mms6 was spread over an area of  $\sim 280$  cm<sup>2</sup> initially and then compressed to  $\sim 105$  cm<sup>2</sup>. The measured normalized XR are shown in part a of Figure 4 with the best-fit model (solid line) obtained from the calculation of the ED profile shown in (b). The reflectivity data are less oscillatory compared to those from lipids or fatty acid monolayers, suggesting lack of a well-defined multilayered structure. Still, the first peak position in reflectivity is shifted to lower  $Q_z$  for the Mms6 film after compression indicating a qualitative increase in the film thickness. The ED profile shows that the distribution of Mms6 varies with surface pressure as the film is compressed to higher surface densities  $\Gamma_s$ . The ED profiles exhibit an asymmetric profile across the interface. In particular, the film/vapor interface is relatively sharp, compared to the film/subphase interface where it is more diffuse especially at high pressures. The volume fraction profiles of Mms6 near the surface characterized by XR are shown in part c of Figure 4. The corresponding amount of adsorbed Mms6 and its thickness are summarized in Table 1.

**Table 1. Thickness and Surface Density of Mms6 Adsorbed on the Aqueous Surface Characterized by XR<sup>a,b</sup>**

amount of deposition ( $\mu$ g)	surface area (cm <sup>2</sup> )	adsorbed layer(s) thickness $\xi$ ( $\text{\AA}$ )	$\Gamma_s$ ( $\times 10^{-4}$ mg/cm <sup>2</sup> )
47	280	$14.8 \pm 0.7$	$1.27 \pm 0.04$
47	105	$31.4 \pm 0.3$	$2.67 \pm 0.08$
50	117	$28.1 \pm 1.6$	$2.64 \pm 0.12$

<sup>a</sup>The upper and lower bounds correspond to 50% increase from  $\chi^2_{\text{min}}$ .

<sup>b</sup>The protein film thickness,  $\xi$ , is estimated as  $\int \Phi_{\text{Mms6}}(z) dz / \Phi_{\text{max}}$  where  $\Phi_{\text{max}}$  is the maximum of  $\Phi_{\text{Mms6}}(z)$ .

By comparing the adsorption of Mms6 at two stages, that is spreading and compression, it can be concluded that about  $\sim 20\%$  of Mms6 desorbed into subphase at each stage. As the adsorbed Mms6 layer(s) is assumed to contain only Mms6 and the subphase solution, the adsorptions  $\Gamma_s$  obtained following eq 2 serves as the lower bound of the actual ones.<sup>23</sup> Therefore, the amount of iron bound to each Mms6 molecule determined

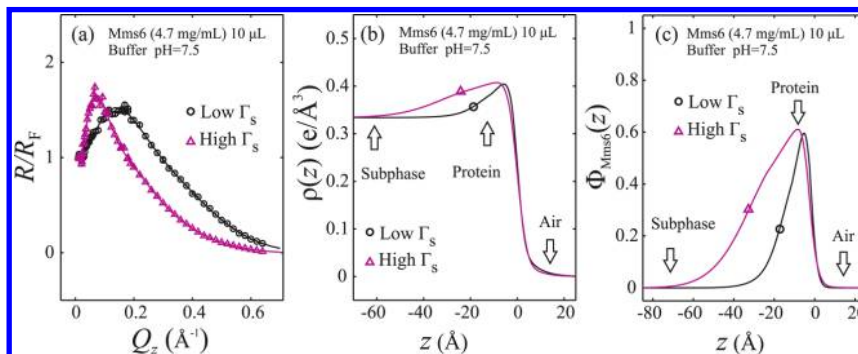


**Figure 4.** (Color online) (a) Measured reflectivity data (symbols) of Mms6 on aqueous surfaces with different surface density. The solid lines are calculated reflectivity based on best-fit parameters. (b) Corresponding ED profiles generated by best-fit parameters. (c) Corresponding volume fraction profiles obtained using eq 2.

by XR and XF may be underestimated by as much as  $\sim 40\%$  if assuming all the proteins stay on the surface. The volume fraction profiles also suggest that the protein conformation changes upon surface compression. When Mms6 is spread on the liquid surface, it is likely that the polypeptide backbone unfolds and lies at the interfaces with the hydrophilic and hydrophobic segments protruding into and away from the aqueous medium, respectively.<sup>19</sup> This is reminiscent of anchor-buoy for adsorption of copolymer with insoluble segments as anchors at the liquid surface and soluble segments as buoys extending into subphase.<sup>40,41</sup> Figure 5

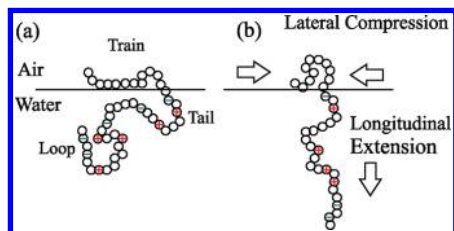


**Figure 5.** Schematic illustration of Mms6 as a flexible polymer chain adsorbed on an aqueous surface. Each circle represents an amino acid residue. “+” and “-” symbols represent the charge carried by protonated/deprotonated side chains. The hydrophobic segments, that is the N-terminals, tend to stay away from the aqueous medium, whereas hydrophilic segments, that is the C-terminals, tend to immerse into the aqueous media. (a) When uncompressed, the Mms6 molecules tend to be spread out on surfaces. (b) Upon lateral compression, the protein laterally contracts and longitudinally extends into subphase to reach new equilibrium conformations.

depicts a simplified arrangement of such a polymer or polypeptide at two surface densities as measured by XR (Figure 4).

The  $R/R_F$  data from Mms6 films in the absence and presence of  $\text{FeCl}_3$  and their corresponding ED profiles are shown in parts a and b of Figure 6, as indicated. Similar control measurements from AA monolayers are shown in parts c and d of Figure 6. They both show that on iron-containing solutions the  $R/R_F$  data are significantly higher compared to those without iron in solutions. The change in ED upon iron binding within the Mms6 suggests intermixing of iron aggregates and Mms6. However, the AA monolayer on the buffered  $\text{FeCl}_3$  solution binds multilayer iron aggregates that protrude into the subphase, as evidenced in (part d of Figure 6). By contrast, on the nonbuffered  $\text{FeCl}_3$ , the iron binding is moderate as evidenced by the significant yet confined increase in ED in the headgroup strata.

Figure 7 shows the normalized reflectivity curves from Mms6 over buffered  $\text{FeCl}_3$  and  $\text{FeCl}_2$  solutions together with their corresponding ED profiles. The ED profiles show that ED is much higher near the surface for Mms6/ $\text{FeCl}_3$  than Mms6/ $\text{FeCl}_2$  indicating there is less iron binding to Mms6 in ferrous iron solutions compared to ferric iron solutions. If the adsorbed layer(s) consists of subphase solution, Mms6 and iron (bare iron ions or iron aggregates), eq 2 can be generalized to

$$\Phi^*(z) \equiv \frac{\rho(z) - \rho_{\text{ref}}(z)}{\rho_{\text{protein}} - \rho_{\text{ref}}(z)} \\ = \Phi_{\text{Mms6}}(z) + \Phi_{\text{Fe}}(z) \frac{\rho_{\text{Fe}} - \rho_{\text{ref}}(z)}{\rho_{\text{protein}} - \rho_{\text{ref}}(z)} \quad (5)$$

where  $\rho_{\text{Fe}}$  and  $\Phi_{\text{Fe}}(z)$  are the ED and volume fraction profile for iron.  $\Phi^*(z)$  is referred to as the nominal volume fraction profile. If the amount of adsorbed Mms6 (proportional

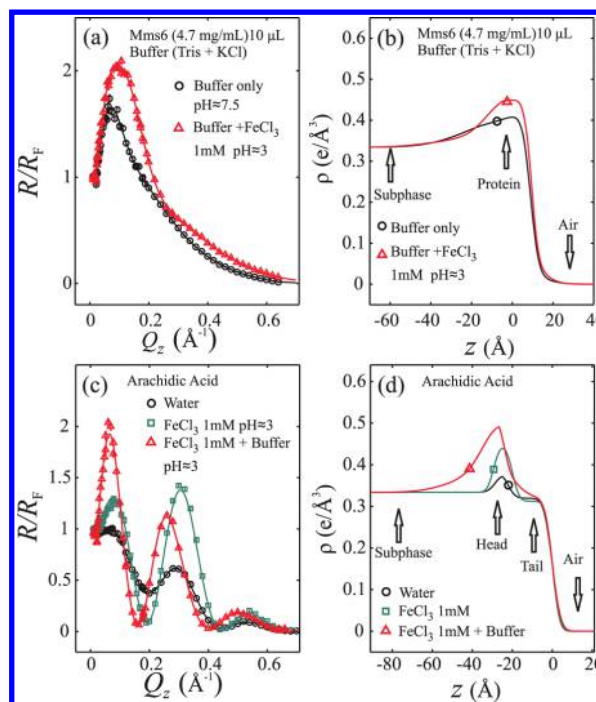


**Figure 6.** (Color online) Reflectivity data (symbols) for (a) an Mms6 film (c) a densely packed AA monolayer on various bulk solutions. (b) and (d) are corresponding ED profiles as indicated. The ED profiles are horizontally shifted for clarity. Best-fit parameters are used to calculate the reflectivity and produce ED profiles (solid lines).

to  $\int \Phi_{\text{Mms6}}(z) dz$ ) remains the same with or without the presence of iron, the increase in area under  $\Phi^*(z)$ , as shown in part c of Figure 7, is proportional to the amount of iron aggregates bound within Mms6 according to eq 5. However, even if this assumption holds true,  $\int \Phi_{\text{Mms6}}(z) dz$  tends to decrease if the Mms6 becomes more compact upon binding with iron aggregates, which defies an exact determination of the amount of bound iron. Further quantitative results on iron binding are discussed in fluorescence section.

**X-ray Fluorescence.** The fluorescence intensity spectra from surface bound iron atoms are obtained by integrating the fluorescence signals below the critical angle  $\alpha_c$  as shown in part a of Figure 8. The intensities of iron characteristic emission lines  $K_\alpha$  and  $K_\beta$  are proportional to the surface density of iron. Iron  $K_\alpha$  and  $K_\beta$  emission lines are prominent for both  $\text{FeCl}_3$  and  $\text{FeCl}_2$  solutions only in the presence of the Mms6 film. The intensities of the emission lines in the presence of Mms6 film for  $\text{FeCl}_3$  solution are approximately 3 times that for  $\text{FeCl}_2$ . This is consistent with the analysis of the XR data that show less iron binding to Mms6 in a ferrous iron solution.

To obtain a global fit of the fluorescence over  $\alpha_i$  as shown in part b of Figure 8, a parametrized concentration profile  $n_s(z)$  in accordance with the effective-density model ED can be constructed. The simplest concentration profile  $n_s(z)$ , that is a Dirac- $\delta$  function that is appropriate for a thin layer of iron atoms, is used to yield surface density of iron.<sup>9,10</sup> The best model fits to the  $Q_z$  dependent fluorescence intensity in terms of the  $K_\alpha$  emission line of iron are shown by solid lines in part b of Figure 8. The detailed analysis yields that, within 30% relative error, the surface density of iron is  $\sim 0.13$  and  $\sim 0.03 \text{ \AA}^{-2}$  for  $\text{FeCl}_3$  and  $\text{FeCl}_2$  buffer solutions corresponding to  $68 \pm 27$  and  $16 \pm 6$  Fe atoms per protein molecule respectively assuming at most 40% desorption of Mms6 from surface.

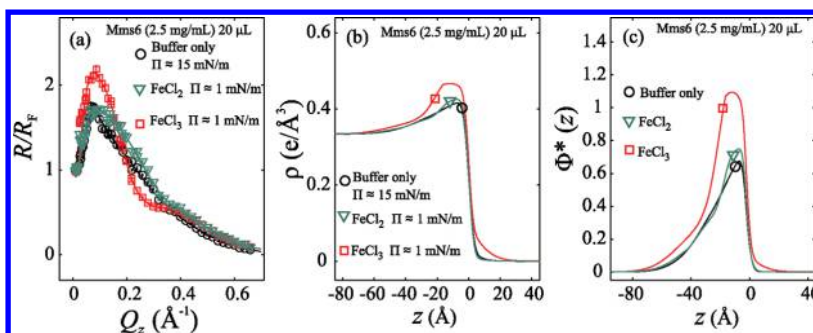


**Figure 7.** (Color online) Reflectivity measurements for 20  $\mu\text{L}$  Mms6 (2.5 mg/mL) spread on pure Tris-KCl buffer solution (pH  $\sim 7.5$ ), 1 mM  $\text{FeCl}_3$  and 1 mM  $\text{FeCl}_2$  subphase solution (pH  $\sim 3.0$ ) after surface compression to the area of  $\sim 117 \text{ cm}^2$ . (a)  $R/R_F$  (symbols), (b) corresponding ED profiles. Best-fit parameters are used to calculate the reflectivity and produce ED profiles (solid lines). (c) The corresponding nominal volume fraction profiles  $\Phi^*(z)$  according to eq 5.

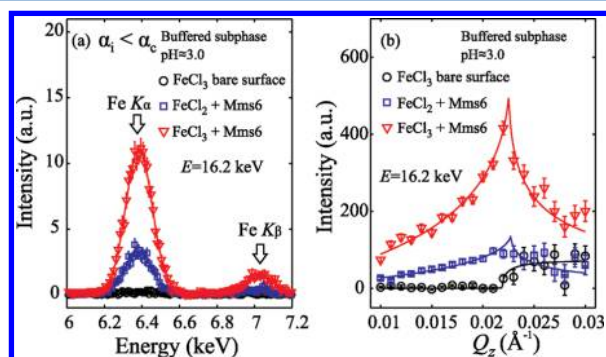


**Figure 8.** (Color online) Fluorescence measurements from 20  $\mu\text{L}$  Mms6 (2.5 g/L) over surface area of  $\sim 117 \text{ cm}^2$ . (a) Fluorescence intensity (symbols) integrated below the critical angle  $\alpha_c$  (over  $Q_z = 0.01\text{--}0.021 \text{ \AA}^{-1}$ ) for 1 mM buffered  $\text{FeCl}_3$  or  $\text{FeCl}_2$  covered by Mms6 film and bare buffered 1 mM  $\text{FeCl}_3$ . Iron  $K_\alpha$  and  $K_\beta$  emission lines are curve-fit with two well-separate Gaussian functions (solid lines). (b) Fluorescence intensity (symbols) as a function of  $Q_z$ . Each data point is the intensity integrated over the Fe  $K_\alpha$  emission line from 6.1 to 6.7 keV. Circle, square, and triangle symbols represent the fluorescence intensity from bulk solution of  $\text{FeCl}_3$  (1 mM) (curve-fit with  $I_b(\alpha_c)$  in eq 3), ion-enriched surface (curve-fit with  $I_s(\alpha_c)$  in eq 3) of  $\text{FeCl}_2$  (1 mM) and  $\text{FeCl}_3$  (1 mM) in the presence of Mms6 film as indicated, respectively. Each error bar represents one standard deviation due to counting statistics. Solid line through symbols are calculated using best-fit parameters. Measurements were conducted at APS (incident X-ray energy  $E = 16.2 \text{ keV}$ ).

The X-ray experiments carried out on AA under same subphase conditions show that high concentration of Tris (20 mM), as is present in the current buffer solution, facilitates the formation of ferric iron (hydr)oxides in the Tris-KCl buffered 1 mM  $\text{FeCl}_3$  or  $\text{FeCl}_2$  solutions and multilayer iron (hydr)oxides under a Langmuir monolayer, as shown in parts c and d of Figure 6. Therefore, we argue that the iron atoms bound to the Mms6 film using  $\text{FeCl}_2$  solution may be those of the  $\text{Fe(III)}$  (hydr)oxides due to the partial oxidation of  $\text{Fe(II)}$  ions and the ensuing formation of  $\text{Fe(III)}$  aggregates in the bulk solution. Control experiments were conducted to minimize the effects of buffer and oxidation. The buffer solution was made using only 100 mM KCl, excluding Tris. To minimize oxidation of  $\text{Fe(II)}$ , argon gas was purged over the solution flasks throughout the process of sample preparation. In addition, the solutions were acidified before the addition of iron salts. The concentration of iron was kept as low as 5  $\mu\text{M}$  for both  $\text{FeCl}_3$  and  $\text{FeCl}_2$  solutions. This protocol significantly slows down the oxidation of ferrous iron and its ensuing formation of  $\text{Fe(III)}$  (hydr)oxides. Figure 9 compares the

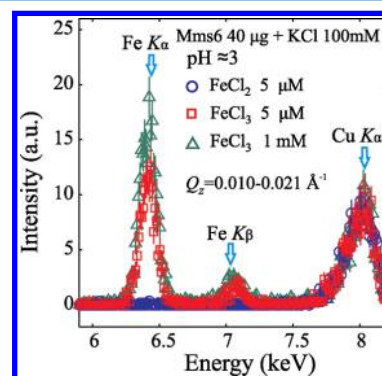


**Figure 9.** (Color online) Fluorescence signal (symbols) integrated below the critical angle  $\alpha_c$  for 40  $\mu\text{L}$  Mms6 (1 mg/mL) spread on surfaces of various iron subphases as indicated. Each point of intensity is an integration over  $Q_z = 0.01\text{--}0.021 \text{ \AA}^{-1}$ . The symbols of squares, circles, and triangles represent the fluorescence data from  $\text{FeCl}_3$  of concentration  $5 \times 10^{-6} \text{ M}$ ,  $\text{FeCl}_2$  of concentration  $5 \times 10^{-6} \text{ M}$ , and  $\text{FeCl}_3$  of concentration  $10^{-3} \text{ M}$ , respectively. Solutions are prepared with 100 mM KCl, excluding Tris. Fluorescence measurements were conducted using in-house LSS at  $E = 8.05 \text{ keV}$ .

fluorescence intensity spectra integrated below the critical angle. It can be seen that fluorescence from surface bound iron atoms almost saturate for 5  $\mu\text{M}$   $\text{FeCl}_3$  solutions compared to 1 mM  $\text{FeCl}_3$  solutions, whereas the surface density of surface bound iron is below the detection limit for  $\text{FeCl}_2$ . That the surface bound iron is ferric rather than ferrous in a ferrous iron solution is further discussed in XANES section.

The bulk pH can regulate the ionic binding of Mms6 protein film. This is illustrated by the results of fluorescence measurements from Mms6 spread over  $\text{LaCl}_3$  solutions. Part a of Figure 10 shows the fluorescence intensity spectra integrated below critical angle for Mms6 spread on 10 mM buffered  $\text{LaCl}_3$  solutions at pH 7 and 4.5 indicating that  $\text{La}^{3+}$  ions accumulate at the surface and give rise to surface fluorescence at pH 7, whereas the surface density of  $\text{La}^{3+}$  ions is below the detection limit at pH 4.5. As the lanthanum manifests itself as a free, positively charged, aqueous trivalent ion in solutions within the pH range investigated in the presence of a film of carboxyl groups,<sup>9,10</sup> it can be concluded that the Mms6 film is analogous to a negatively charged interface, the surface charge density of which is regulated by the bulk pH. This is also consistent with the isotherms results, as shown in part b of Figure 3. We conclude that it is the Coulombic force that drives  $\text{La}^{3+}$  to rise to the surface to neutralize negatively charged Mms6.



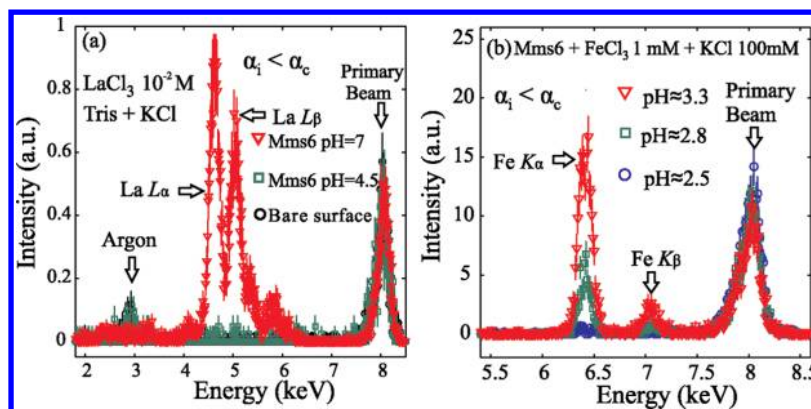


**Figure 10.** (Color online) Integrated fluorescence intensity spectra below the critical angle  $\alpha_c$  from ions at the surface. Each point of intensity is an integration over  $Q_z = 0.01\text{--}0.021 \text{ \AA}^{-1}$ . (a) The symbols of circles, squares and triangles represent the fluorescence data from bare buffered  $\text{LaCl}_3$  solution, buffered  $\text{LaCl}_3$  solution covered with Mms6 at pH 4.5 and 7.0, respectively. (b)  $40 \mu\text{L}$  Mms6 (1 mg/mL) spread on surfaces ( $\sim 117 \text{ cm}^2$ ) of 1 mL  $\text{FeCl}_3$  solutions buffered with 100 mM KCl (excluding Tris). The symbols of circles, squares and triangles represent the fluorescence data from  $\text{FeCl}_3$  solution as subphase covered by Mms6 at pH 2.5, 2.8, and 3.3, respectively. Fluorescence measurements were conducted using in-house LSS at  $E = 8.05 \text{ keV}$ .

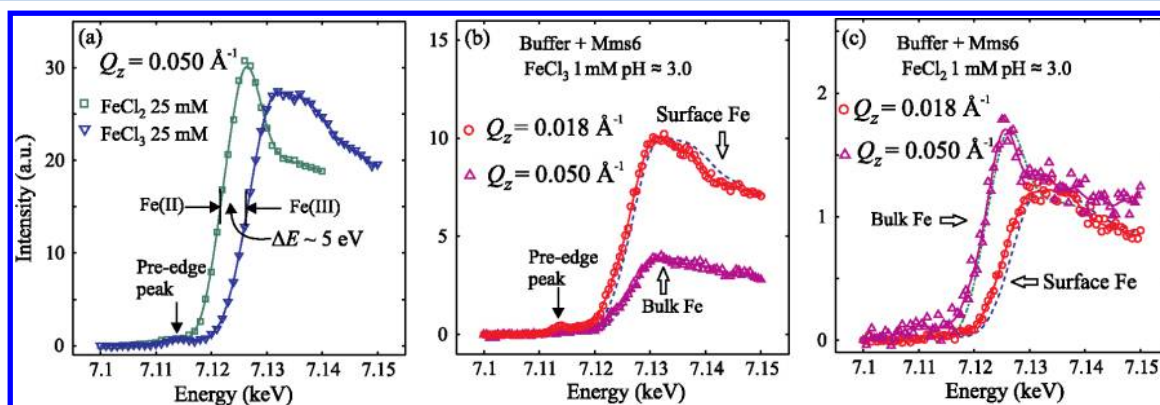


**Figure 11.** (Color online) XANES spectra for iron under various conditions. (a) The XANES spectra for  $\text{FeCl}_3$  and  $\text{FeCl}_2$  solutions at  $Q_z = 0.05 \text{ \AA}^{-1}$ . Both concentrations are 25 mM. The position of the rising absorption edge corresponds to the sharpest slope. The energy gap ( $\Delta E$ ) between two absorption edges for  $\text{Fe(III)}$  and  $\text{Fe(II)}$  is approximately 5 eV. (b) and (c) are the XANES spectra for  $\text{FeCl}_3$  and  $\text{FeCl}_2$  solutions in the presence of Mms6 and Tris-KCl-HCl buffer, respectively. The spectra were obtained at  $Q_z = 0.018 \text{ \AA}^{-1}$  and  $0.050 \text{ \AA}^{-1}$  sequentially. The dashed lines in (b) and (c) are the rescaled XANES curves from (a) for bulk  $\text{FeCl}_3$  solution. The dashed-dotted line in (c) is the rescaled XANES curve from (a) for bulk  $\text{FeCl}_2$  solution.

Similar fluorescence measurements from  $40 \mu\text{g}$  Mms6 over surface area ( $\sim 117 \text{ cm}^2$ ) of 1 mM  $\text{FeCl}_3$  at various pH are shown in part b of Figure 10. These iron solutions were prepared excluding Tris for the reason discussed above. Assuming at most 40% (20% in deposition and 20% in compression) of Mms6 lost in the process of deposition and compression, the molecular area of Mms6 proteins may vary from  $\sim 480$  to  $\sim 800 \text{ \AA}^2$ . The obtained surface density of iron, within 30% relative error, is  $\sim 0.034$  and  $0.012 \text{ \AA}^{-2}$ , corresponding to  $22 \pm 8$  and  $8 \pm 3$  Fe atoms per molecule for pH 3.3 and 2.8, respectively. That corresponds well with the recently reported value of  $\sim 19$  Fe per Mms6 molecule at pH  $\sim 3$ .<sup>15</sup> At pH 2.5, the surface density of iron is below our detection limit. The observation that the fluorescence intensity from surface bound iron increases with pH suggests that the higher pH results in more iron binding. In the  $\text{FeCl}_3$  solutions within the pH range investigated (pH  $\sim 2.2\text{--}3.5$ ), most  $\text{Fe(III)}$  atoms form iron (hydr)oxides and are positively charged.<sup>9,10,42</sup> It has been reported that the isoelectric point of Mms6 suspended in solutions, obtained by the zeta potential measurements, is pH  $\sim 3.6$ , below which its net surface charge density becomes positive.<sup>6</sup> As iron binding was observed at pH  $\sim 2.8$  (part b of Figure 10), the isoelectric point

of the surface bound Mms6 may be shifted to a lower pH ( $< 2.8$ ), which is analogous to an AA monolayer/ion system due to the collective behavior of the anions (carboxyl groups) at the interface.<sup>9,10,43</sup>

**XANES.** XANES spectra, obtained by integrating over the iron  $K_\alpha$  emission lines as a function of incident X-ray energy  $E$  at constant  $Q_z$  (measured above the critical angle at  $Q_z = 0.05 \text{ \AA}^{-1}$ ) for bulk ions of  $\text{FeCl}_3$  and  $\text{FeCl}_2$  solutions of bare surfaces, are shown in part a of Figure 11. The rising absorption edge arises from the electronic transition from  $1s \rightarrow 4p$  in Fe outer shell electronic configuration. The XANES spectra of bulk  $\text{Fe(III)}$  and  $\text{Fe(II)}$  exhibit a significant  $\sim 5 \text{ eV}$  shift for the rising absorption edge (corresponding to the position of the maximum slope, as indicated in part a of Figure 11). This shift can be used to distinguish  $\text{Fe(II)}$  and  $\text{Fe(III)}$ . In the case of  $\text{FeCl}_3$ , there is an additional weak pre-edge peak due to the  $1s \rightarrow 3d$  transition.<sup>44</sup> The shape above the absorption edge is different for the two ions in water solutions due to the combined effect of electronic configuration and the coordination of ligands around the ion. We use these two spectra of bulk iron after rescaling for comparison with spectra from surface bound iron to evaluate their oxidation states as  $\text{Fe(III)}$ ,  $\text{Fe(II)}$ , or an intermediate



between these two states. For the Tris-KCl buffered iron solution, the XANES from the iron constituents in the bulk remain nearly identical to the rescaled XANES spectra as shown in parts b and c of Figure 11, which suggests that the bulk properties are the same in the presence of both buffer and Mms6 film at the surface. However, both XANES spectra from the surface-bound iron in buffered FeCl<sub>3</sub> and FeCl<sub>2</sub> solutions are to a good approximation similar to that for the bulk Fe(III), with probable differences in the details of local coordination giving rise to a minor difference in spectral shape above the absorption edge. This result indicates that under our experimental conditions, the bound iron atoms tend to be in oxidation state +3 even though the subphase is abundant in Fe(II). This can be the result of the strong tendency of Fe(II) to oxidize to Fe(III) (in untreated aqueous solution) that leads to subsequent formation of Fe(III) aggregates and binding to Mms6. This may also result from oxidation of Fe(II) at the surface.

## CONCLUSIONS

Using surface sensitive X-ray scattering and spectroscopic techniques, we explored the behavior of Mms6 as a film on buffer solutions. Our results are summarized as follows: 1) Mms6 proteins form a stable monomolecular layer at the liquid/vapor interface. Film compressions cause conformational changes so that the molecules laterally contract and extend into the solution. 2) Ferric iron ions and iron aggregates in solution readily bind to Mms6 films and the binding saturates at about  $\sim 10 \mu\text{M}$ . 3) Whereas Mms6 strongly binds to Fe(III) at low pH, it weakly binds to Fe(II) or La(III) under the same conditions. However, at higher pH ( $\sim 7$ ), significant La<sup>3+</sup> binding is observed. This behavior is reminiscent of iron binding to the fatty acid AA monolayers that form a perfect carboxylic template.

## ASSOCIATED CONTENT

### Supporting Information

Analysis of X-ray reflectivity. This material is available free of charge via the Internet at <http://pubs.acs.org>.

## AUTHOR INFORMATION

### Corresponding Author

\*E-mail: [vaknin@ameslab.gov](mailto:vaknin@ameslab.gov).

### Notes

The authors declare no competing financial interest.

## ACKNOWLEDGMENTS

We thank A. Travesset for stimulating discussions, and N.A. Anderson, R.Y. Park, K. Flores, J. Pleasant, and D. Robinson for the technical support. The work at Ames Laboratory and at the Advanced Photon Source were supported by the Department of Energy, Office of Basic Energy Sciences under contracts numbers DE-AC02-07CH11358 and DE-AC02-06CH11357, respectively.

## REFERENCES

- (1) Cornell, R. M.; Schwertmann, U. *The Iron Oxides: Structure, Properties, Reactions, Occurrences and Uses*; VCH Publishers: New York, NY, 1996.
- (2) Laurent, S.; Forge, D.; Port, M.; Roch, A.; Robic, C.; Elst, L. V.; Muller, R. N. *Chem. Rev.* **2008**, *108*, 2064.
- (3) Komeili, A. *Annu. Rev. Biochem.* **2007**, *76*, 351.
- (4) Arakaki, A.; Webb, J.; Matsunaga, T. *J. Biol. Chem.* **2003**, *278*, 8745.
- (5) Arakaki, A.; Nakazawa, H.; Nemoto, M.; Mori, T.; Matsunaga, T. *J. R. Soc. Interface* **2008**, *5*, 977.
- (6) Amemiya, Y.; Arakaki, A.; Staniland, S. S.; Tanaka, T.; Matsunaga, T. *Biomaterials* **2007**, *28*, 5381.
- (7) Arakaki, A.; Masuda, F.; Amemiya, Y.; Tanaka, T.; Matsunaga, T. *J. Colloid Interface Sci.* **2010**, *343*, 65.
- (8) Abe, M.; Ishihara, T.; Kitamoto, Y. *J. Appl. Phys.* **1999**, *85*, 5705.
- (9) Wang, W.; Park, R. Y.; Travesset, A.; Vaknin, D. *Phys. Rev. Lett.* **2011**, *106*, 056102.
- (10) Wang, W.; Park, R. Y.; Meyer, D. H.; Travesset, A.; Vaknin, D. *Langmuir* **2011**, *27*, 11917.
- (11) Kang, Y. S.; Lee, D. K.; Lee, C. S. *J. Phys. Chem. B* **2002**, *106*, 9341.
- (12) Degen, P.; Paulus, M.; Maas, M.; Kahner, R.; Schmacke, S.; Struth, B.; Tolan, M.; Rehage, H. *Langmuir* **2008**, *24*, 12958.
- (13) Sarkar, R.; Pal, P.; Mahato, M.; Kamilya, T.; Chaudhuri, A.; Talapatra, G. B. *Colloid. Surf. B: Biointerface* **2010**, *79*, 384.
- (14) Arakaki, A.; Masuda, F.; Matsunaga, T. *MRS Proceedings* **2009**, 1187.
- (15) Wang, L.; Prozorov, T.; Palo, P. E.; Liu, X.; Vaknin, D.; Prozorov, R.; Mallapragada, S.; Nilsen-Hamilton, M. *Biomacromolecules* **2012**, *13*, 98.
- (16) Langmuir, I.; Schaefer, V. J. *Chem. Rev.* **1939**, *24*, 181.
- (17) Tripp, B. C.; Magda, J. J.; Andrade, J. D. *J. Colloid Interface Sci.* **1995**, *173*, 16.
- (18) Schwenke, K. *Proteins at Liquid Interfaces*; D. Möbius Miller, R., Ed.; Elsevier: 1998; 1–50.
- (19) MacRitchie, F. *Proteins at Liquid Interfaces*; D. Möbius Miller, R., Ed.; Elsevier: 1998; 149–177.
- (20) Vaknin, D.; Als-Nielsen, J.; Piepenstock, M.; Lösche, M. *Biophys. J.* **1991**, *60*, 1545.
- (21) Lösche, M.; Piepenstock, M.; Diederich, A.; Grünwald, T.; Kjaer, K.; Vaknin, D. *Biophys. J.* **1993**, *65*, 2160. and Vaknin, D.; Kjaer, K.; Blankenburg, R.; Ringsdorf, H.; Piepenstock, M.; Diederich, A.; Lösche, M. *Langmuir* **1993**, *9*, 1171.
- (22) Gidalevitz, D.; Huang, Z.; Rice, S. A. *Proc. Natl. Acad. Sci., U.S.A.* **1999**, *96*, 2608.
- (23) Yano, Y. F.; Uruga, T.; Tanida, H.; Toyokawa, H.; Terada, Y.; Takagaki, M.; Yamada, H. *Langmuir* **2009**, *25*, 32.
- (24) Prozorov, T.; Mallapragada, S. M.; Narasimhan, B.; Wang, L.; Palo, P.; Nilsen-Hamilton, M.; Williams, T. J.; Bazylinski, D. A.; Prozorov, R.; Canfield, P. C. *Adv. Funct. Mater.* **2007**, *17*, 951.
- (25) Vaknin, D. *Characterization of Materials*; Kaufmann, E. N., Ed.; John Wiley & Sons: New York, 2003; 1027–1047.
- (26) Parratt, L. G. *Phys. Rev.* **1954**, *59*, 359.
- (27) Tolan, M. *X-ray Scattering from Soft-Matter Thin Films*; Springer-Verlag: Berlin Heidelberg, 1999; 26–31.
- (28) Paulus, M.; Degen, P.; Brenner, T.; Tiemeyer, S.; Struth, B.; Tolan, M.; Rehage, H. *Langmuir* **2010**, *26*, 15945.
- (29) Hüsecken, A. K.; Evers, F.; Czeslik, C.; Tolan, M. *Langmuir* **2010**, *26*, 13429.
- (30) Supporting Information.
- (31) Jackler, G.; Steitz, R.; Czeslik, C. *Langmuir* **2002**, *18*, 6565.
- (32) Evers, F.; Shokuie, K.; Paulus, M.; Sternmann, C.; Czeslik, C.; Tolan, M. *Langmuir* **2008**, *24*, 10216.
- (33) Fischer, H.; Polikarpov, I.; Craievich, A. *Protein Sci.* **2004**, *13*, 2825.
- (34) Bu, W.; Vaknin, D. *J. Appl. Phys.* **2009**, *105*, 084911.
- (35) Yun, B.; Bloch, J. M. *J. Appl. Phys.* **1990**, *68*, 1421.
- (36) Daillant, J.; Bosio, L.; Benattar, J. J.; Blot, C. *Langmuir* **1991**, *7*, 611.
- (37) Als-Nielsen, J.; McMorrow, D. *Elements of modern X-ray Physics*, John Wiley & Sons Ltd: England, 2001.
- (38) Daillant, J. *X-ray and Neutron Reflectivity: Principles and Applications*, Springer: Germany, 1999.
- (39) Bu, W.; Flores, K.; Pleasants, J.; Vaknin, D. *Langmuir* **2009**, *25*, 1068.
- (40) de Gennes, P. G. *Adv. Colloid Interface Sci.* **1987**, *27*, 189.

- (41) Jones, R. A.; Richards, R. W. *Polymers at Surface and Interfaces*; Cambridge University Press, 187–240, 1999.
- (42) Kosmulski, M. *J. Colloid Interface Sci.* **2002**, 253, 77.
- (43) Travesset, A.; Vaknin, D. *Europhys. Lett.* **2006**, 74, 181.
- (44) Shulman, R. G.; Yafet, Y.; Eisenberger, P.; Blumberg, W. E. *Proc. Natl. Acad. Sci., U.S.A.* **1976**, 73, 1384.